Eleventh International Conference on Computational Fluid Dynamics (ICCFD11), Maui, HI, USA, July 11-15, 2022

ICCFD11-2022-2102

All-speed Multi-phase Computational Framework for Simulating the Entire Process of Underwater Explosions: Shocks, Cavitations, and Bubble Pulsations

Kyungjun Choi* and Chongam Kim*,**
Corresponding author: chongam@snu.ac.kr

* Department of Aerospace Engineering, Seoul National University, Korea
** Institute of Advanced Aerospace Technology, Seoul National University, Korea

Abstract: Underwater explosions are composed of three distinct physical phenomena: (I) initial shock wave, (II) bulk cavitation, and (III) pulsation of the explosion gas bubble, with each stage inducing a respective impact load on the surrounding structure. While actual events are sequential and continuous, previous research has focused on each stage separately, ignoring potential interactions between each stage. This paper proposes a high-fidelity computational framework capturing the significant flow physics of an underwater explosion's entire process. More emphasis has been placed on accurate thermodynamic aspects, such as sophisticated equation of state and thermodynamic cavitation process. The framework's applicability is discussed by comparing computations to field experimental references. An initial state of the explosion bubble is configured to provide a realistic amount of shock wave intensity (Stage I). The prediction accuracy for the bulk cavitation (Stage II) is greatly improved by adopting the thermodynamic cavitation process in terms of the intensity and the time of incident. The explosion bubble's periodical pulsation (Stage III) is well captured, and Rayleigh-Taylor instability is observed due to a sharp representation of the phase interface.

Keywords: Underwater Explosions, Computational Fluid Dynamics, Multi-phase Flows, Shock Waves, Cavitation, Bubble Pulsations.

1 Introduction

Underwater explosion (UNDEX) refers to the detonation of explosive charges immersed in water. While the UNDEX scenario is seemingly simple, actual physical phenomena beneath the water's surface are highly complex and can be categorized into three stages as in Fig. 1. The massive energy released by the initial explosion causes the propagation of a spherical blast wave (Stage I). Rarefaction waves are reflected after the shock wave reaches the free surface, while a weak shock is transmitted to the air due to an impedance mismatch between air and water media. As the expansion waves propagate in the water, cavitation bubble clusters are formed in the low-pressure region beneath the free surface (Stage II). The moment the cavity clusters collapse, a bulk cavitation load arises that could reach a comparable magnitude to Stage I. Meanwhile, the explosion gas bubble expands and contracts periodically, emitting a large amount of pressure pulses (Stage III). The actions of theses multiple dynamic loads by shock, bulk cavitation collapse, and bubble pulses damage any structures near the explosion.

With many different efforts since the 1940s, the major process of UNDEX has been quite well understood. The theoretical methods have been developed from establishing semi-empirical formulas to bubble motion equations. Based on a series of experiments, Cole [1] proposed widely-accepted relationships for the intensity of a shock wave or the maximum bubble radius. The theoretical analyses of bubble motion began with the work of Rayleigh and Plesset [2, 3], and the original equation of motion has been improved by taking into

account the effect of liquid compressibility, gravity, viscosity, and heat transfer [4, 5, 6]. However, analytic methods for studying UNDEX are typically appropriate for bubbles with small deformations [7].

A number of experimental studies on shock wave propagation and bubble dynamics have been conducted. Swift and Decius [8] carried out a UNDEX experiment with TNT charge in deep water ranging from 100 to 200 m in a variety of explosive sizes. The photographic records were used to calculate the bubble's growth and decay over time, while the piezoelectric gauge was used to measure the shock wave history. Gaspin [9] conducted a field test with Pentolite explosives (a 50/50 mixture of TNT and PETN) to record the pressure histories of primary shock wave loads and bulk cavitation loads. The report also describes the occurrence of a visually confirmed bulk cavity. Small size explosives in the shallow water or near a solid structure have been used to study the boundary effects on bubble dynamics in recent years [10, 11]. However in experiments, sensors are often damaged by the explosion, the protection for sensors may affect the measurements [12], and the wire harness may be moved by the current [8]. Furthermore, because of the potential risk to humans as well as the ocean environment, most experiments have been limited to model scale or the electric spark-generated bubble. Unlike bubbles generated from other sources such as a laser, electrical discharge, or ultrasound into the liquid, underwater explosion bubbles have distinct physical characteristics: a high initial pressure and temperature, a complex gas composition, and a significant amount of shock wave emission. As direct scaling up to the real scale is difficult due to gravity playing an important role, numerical approaches which are not restricted by physical scale have strong advantages with the capability of flow visualizations and data acquisitions.

A number of numerical simulations in the literature have adopted the boundary integral method (BIM). BIM is effective in predicting the bubble dynamics itself because only velocity potential is computed at the bubble surface. The interaction of the explosion bubble with the surrounding boundaries, as well as topology change has received a lot of attention [13, 14, 15, 16]. However, based on the assumption of potential flow, BIM has limitations in predicting the entire flow fields with shock and phase change.

A computational fluid dynamics (CFD)-based numerical simulations adopting more realistic Euler or Navier-Stokes equations are becoming increasingly popular due to their capability to capture the details of the flow phenomena underlying UNDEX. Most of the CFD computations, however, have focused on each phase of the UNDEX scenario separately, capturing the shock wave propagation near the boundary or the explosion bubble behavior itself [12, 17]. Since physical phenomena of UNDEX take place consecutively (Stage I $\rightarrow$ III), the possible interactions between stages must be considered by a continuous simulation of the entire process, especially in the case of an explosion close to the boundary or multiple detonations. Previous numerical studies had limitations due to the use of simplified equations of state (EOS) and pressure-cut or mechanical cavitation model [18, 19, 20, 21]. According to Pelanti [20], the thermodynamic cavitation process, which reflects mass transfer and heat exchange between the liquid and vapor phases, has a significant influence in predicting the pressure distribution in the cavity region. As a result, the objective of this research is to propose, validate, and demonstrate a high-fidelity computational framework that can accurately reproduce the major flow physics of the entire three stages of UNDEX. The solver's requirements are proposed and validated with experimental references.

The present paper is organized as follows. After the introduction, a detailed description of the computational framework is given in Section 2. Section 3 presents numerical results and discusses the program's performance. Section 4 concludes with closing remarks.

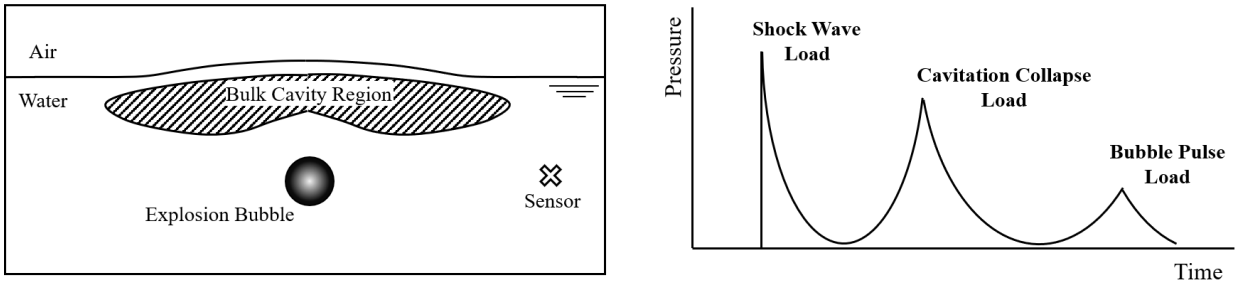

Figure 1: Schematic diagram of the underwater explosion event.

2 Computational Framework

The following requirements were considered in order to simulate the entire UNDEX process.

- A multi-phase flow model capable of describing at least three phases is required for a realistic simulation of UNDEX. A non-condensable gas phase of the explosion bubble, the liquid phase of water are present initially, and the vapor phase of water is created by the cavitation. If the explosion happens near the free surface as in Fig. 1, there should be a fourth phase of air. In order to employ separate EOS for the explosion bubble and air, the numerical model should be able to handle four different phases (here, "phase" is used as a common term for indicating different phases and/or species). To accurately predict the propagation of shock waves correctly, the multi-phase model should be in a conservative form.

- As a result of the explosion, the flow field undergoes variations in flow conditions spanning from ambient to high pressure and temperature. As generally known, the simple equation form of EOS covers only a limited range, and the choice of EOS can affect the bubble period, shock speed, or strength [22, 23]. In order to reflect accurate fluid properties over a wide range of pressure and temperature variations, real-fluid EOS is required.

- A thermodynamic cavitation model is required for liquid-vapor transition in the cavitation region. In most results of UNDEX simulations published in the literature, the vapor phase is not generated because pressure-cut or mechanical cavitation models are used. Liquid water should be vaporized and condensed back according to the local pressure and temperature during the computations, with latent heat going in and out along the thermodynamic cavitation process.

- Other numerical techniques for accuracy and efficiency of computation will also be necessary, such as low Mach number preconditioning for all-speed flow computations, interface sharpening technique to prevent excessive phase interface diffusion and multi-dimensional limiting process for stable and accurate shock capturing, and parallel computing library for large-scale computations.

An in-house CFD program, ACTFlow_MP, has been developed following the above requirements. This solver is extended from baseline solvers developed and extensively validated by this research group [24, 25]. General descriptions of the program corresponding to the aforementioned conditions are as follows.

2.1 Governing Equations

The current study employs a homogeneous mixture model for the multi-phase flow model. In the homogeneous mixture approach, mechanical (velocity and pressure) and thermal (temperature) equilibrium assumptions are brought between phases on each computational cell. This model is advantageous in that it secures the issue of conservation and hyperbolicity, ensuring the Rankine-Hugoniot shock jump condition, thereby facilitating the numerical schemes developed for single-phase gas dynamics. The fluid mixture is described by one set of the continuity, momentum, and energy equations. An additional continuity equation is required to account for the mixture composition in the metastable equilibrium state; thus, extra three continuity equations are implemented to handle four phases. Since the underwater explosion is an inertia-dominant phenomenon, the viscosity is found to play a negligible role during the overall event, which comes into inviscid flow characteristics [26, 27]. The governing equations are then transformed into two-dimensional axisymmetric compressible Euler equations:

$$\frac{\partial}{\partial t}\int_{\Omega}\vec{W}r\mathrm{d}\Omega+\oint_{\partial\Omega}\vec{F}r\mathrm{d}S=\int_{\Omega}\vec{S}r\mathrm{d}\Omega, \tag{1}$$

where the radius r is a distance in the radial direction from the axis. The vector of conservative variable $\vec{W}$ and the convective flux vector $\vec{F}$ are respectively given by

$$\vec{W}=\left[\rho \quad \rho u \quad \rho v \quad \rho E \quad \rho y_{\mathrm{v}} \quad \rho y_{\mathrm{g1}} \quad \rho y_{\mathrm{g2}}\right]^{\mathrm{T}}, \tag{2}$$

$$\vec{F}=\left[\rho U \quad \rho uU+n_x p \quad \rho vU+n_r p \quad \rho HU \quad \rho y_{\mathrm{v}}U \quad \rho y_{\mathrm{g1}}U \quad \rho y_{\mathrm{g2}}U\right]^{\mathrm{T}}. \tag{3}$$

Here, $\vec{S}$ represent the source term vector, which is made up of sources for axisymmetric effect $\vec{S}_{\text{axisymmetric}}$, gravitational force $\vec{S}_{\text{gravity}}$ and phase change rate $\vec{S}_{\text{cavitation}}$.

$$\vec{S}_{\text{axisymmetric}} = \frac{1}{r}\left[0 \quad 0 \quad p \quad 0 \quad 0 \quad 0 \quad 0\right]^{\mathrm{T}}, \tag{4}$$

$$\vec{S}_{\text{gravity}} = \left[0 \quad \rho g_x \quad 0 \quad \rho g_x u \quad 0 \quad 0 \quad 0\right]^{\mathrm{T}},$$

$$\vec{S}_{\text{cavitation}} = \left[0 \quad 0 \quad 0 \quad 0 \quad \dot{m}_{\text{evaporation}} - \dot{m}_{\text{condensation}} \quad 0 \quad 0\right]^{\mathrm{T}},$$

where g_x refers to the acceleration of gravity.

The contravariant velocity $U(\equiv n_x u + n_r v)$ refers to the velocity component normal to the surface element $\mathrm{d}S$. The mass fractions in a computational cell satisfy the following constitutive relation:

$$y_\ell + y_{\mathrm{v}} + y_{\mathrm{g1}} + y_{\mathrm{g2}} = 1, \tag{5}$$

where the subscripts $(\ell, \mathrm{v}, \mathrm{g1}, \mathrm{g2})$ correspond to the liquid, vapor phase of the water, and non-condensable gas of fluid 1 and 2, respectively.

In order to handle flows with Mach numbers ranging from subsonic to supersonic, the governing equations are preconditioned using the Weiss and Smith preconditioned matrix $\mathbf{\Gamma}$ [28]. The dual-time stepping method is used for unsteady computations, as shown below:

$$\mathbf{\Gamma}\frac{\partial}{\partial \tau}\int_\Omega \vec{Q} r \mathrm{d}\Omega + \frac{\partial}{\partial t}\int_\Omega \vec{W} r \mathrm{d}\Omega + \oint_{\partial\Omega} \vec{F} r \mathrm{d}S = \int_\Omega \vec{S} r \mathrm{d}\Omega, \tag{6}$$

where t denotes the physical time and τ is the pseudo-time used in the sub-iteration procedure. Here, $\vec{Q}$ stands for the vector of primitive variables given by $\vec{Q} = \left[p \quad u \quad v \quad T \quad y_{\mathrm{v}} \quad y_{\mathrm{g1}} \quad y_{\mathrm{g2}}\right]^{\mathrm{T}}$. In case $1/\beta$ inside Γ becomes $\frac{\partial \rho}{\partial p}$, then Γ goes back to the Jacobian matrix $\frac{\partial \vec{W}}{\partial \vec{Q}}$ and Eq. (6) results in a non-preconditioned system in the primitive form.

2.2 Equation of State

The governing equations are closed with equation of state for each component or phase. The mixture density is defined as follows:

$$\frac{1}{\rho} = \frac{1 - y_{\mathrm{v}} - y_{\mathrm{g1}} - y_{\mathrm{g2}}}{\check{\rho}_\ell} + \frac{y_{\mathrm{v}}}{\check{\rho}_{\mathrm{v}}} + \frac{y_{\mathrm{g1}}}{\check{\rho}_{\mathrm{g1}}} + \frac{y_{\mathrm{g2}}}{\check{\rho}_{\mathrm{g2}}}, \tag{7}$$

where $\check{q}$ indicates the quantity q specified in terms of Amagat's law. The mixture enthalpy h is calculated as

$$h = h_\ell(1 - y_{\mathrm{v}} - y_{\mathrm{g1}} - y_{\mathrm{g2}}) + h_{\mathrm{v}} y_{\mathrm{v}} + h_{\mathrm{g1}} y_{\mathrm{g1}} + h_{\mathrm{g2}} y_{\mathrm{g2}}. \tag{8}$$

As a function of local pressure p and temperature T, all thermodynamic properties of each phase are generated as follows:

$$\check{\rho}_i = \check{\rho}_i\left(p, T\right), \quad h_i = h_i\left(p, T\right), \quad \left(i = \ell,\ \mathrm{v},\ \mathrm{g1},\ \mathrm{g2}\right). \tag{9}$$

In order to reflect accurate thermodynamic properties in the UNDEX scenario, separate EOSs are adopted to corresponding fluid phases as in Table 1. The ideal gas law is used for air above the free surface. For the liquid and vapor phases of water, IAPWS-IF97 formulation [29] is employed to account for real-fluid

Table 1: EOSs for corresponding region in UNDEX scenario

Region	**EOS**
Liquid water	IAPWS-IF97 (liquid)
Water vapor	IAPWS-IF97 (vapor)
Explosion gas bubble	Jones-Wilkins-Lee (JWL)
Air above the free surface	Ideal gas law

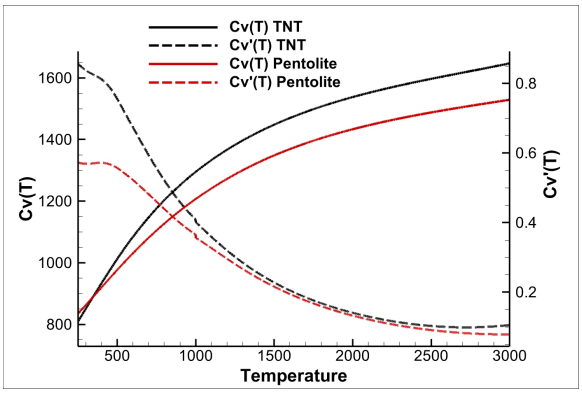

Figure 2: Specific heat of explosion gases

properties and to cover the metastable state as well. For the detonation product inside the gas bubble, Jones-Wilkins-Lee (JWL) EOS [30] is adopted.

2.2.1 Explosion gas modeling

JWL EOS accurately and easily models the pressure generated by chemical energy in an explosion and is widely used in that accuracy and accessibility for various types of explosive materials. The EOS is written as follows:

$$p_{\mathrm{JWL}}(\rho, T) = A\left(1 - \frac{\omega}{R_1 V}\right)\exp(-R_1 V) + B\left(1 - \frac{\omega}{R_2 V}\right)\exp(-R_2 V) + \frac{\omega \rho_0 e}{V}, \tag{10}$$

where A, B, R_1, R_2, ω are material constants [18] and V is the volume ratio of detonation product to the initial state V_{gas}/V_0. The caloric relation between specific energy e and temperature T is required to use JWL EOS in our computational framework.

For the computational efficiency, the detonation product of explosive material is treated as a gas mixture in chemical equilibrium in this work. Because the chemical composition of most C-H-N-O type explosives is known to be frozen below 1800 K, as a result, the chemical balance equation of TNT [31] and Pentolite (50/50 of TNT + PETN) [32] in equilibrium state can be written as follows:

$$\mathrm{TNT}: C_7H_5N_3O_{3(s)} \rightarrow 2.2CO_{(g)} + 1.6H_2O_{(g)} + 1.5N_{2(g)} + 1.1CO_{2(g)} + 0.36H_{2(g)} + 0.27CH_{4(g)} + 3.43C_{(s)}, \tag{11}$$

$$\begin{aligned}\mathrm{Pentolite}: C_{12}H_{13}N_7O_{18(s)} \rightarrow\, & 5.7CO_{(g)} + 5.9H_2O_{(g)} + 3.5N_{2(g)} + 2.9CO_{2(g)} + 0.3H_{2(g)} + 0.07CH_{4(g)} \\ & + 0.05NH_{3(g)} + 3.97C_{(s)},\end{aligned} \tag{12}$$

where the subscript (g) and (s) corresponds to gas and solid state of detonation product.

The specific heat of gas mixture at constant volume $C_{\mathrm{v}}(T)$ is then calculated according to:

$$C_{\mathrm{v,mixture}} = \sum_{i=1}^{n_{\mathrm{gas}}} \frac{(\tilde{C}_{\mathrm{p},i} - R)Y_i}{W_i} + \sum_{j=1}^{n_{\mathrm{condensed}}} \frac{\tilde{C}_{\mathrm{p},j} Y_j}{W_j}, \tag{13}$$

where R is the universal gas constant, Y_i is the mass fraction, and W_i is each species' molecular weight. The condensed product such as carbon is included as part of the fluid phase. The specific heats of each species at constant pressure $\tilde{C}_{\mathrm{p}}(T)$ are calculated using the curve-fitted temperature-dependent functions with nine coefficients [33], and the results are shown in Fig. 2.

2.3 Thermodynamic Cavitation Process

A pressure-cut model is commonly used to account for the cavitation process in a simple way.

$$p_{\text{local}} = \max(p_{\text{local}},\ p_{\text{sat}}(T_{\text{local}})) \tag{14}$$

This model operates by cutting off the cell-averaged pressure value if it is less than the local saturation pressure. However, by restricting the excessive pressure drop only, the density change between liquid and vapor cannot be reflected; density from the liquid water is used in both the liquid and vapor regions.

The present work describes the non-equilibrium phase change process by the source term as in Eq. 2.1. Among various models that provide the finite rate of phase change, the physics-based cavitation model [34] is chosen for the computation. The physics-based cavitation model is developed based on the classical bubble growth theories and successfully captures the phase change phenomena ranging from general water to thermosensitive fluids such as cryogens. The coefficients included in B and η_{cd} are configured in this numerical framework as proposed in [34].

$$\dot{m}_{\text{evap}} = 3\left(\frac{4\pi\left(1-\alpha_{\text{v}}\right)}{3\alpha_{\text{v}}}\frac{B}{3R_{\text{min}}^{3}}\right)^{1/3}\frac{\rho_{\ell}\rho_{\text{v}}\alpha_{\text{v}}\left(1-\alpha_{\text{v}}\right)}{\rho}\min\left(\left|\dot{R}_{\text{i}}\right|,\left|\overline{\dot{R}_{\text{t}}}\right|\right), \tag{15}$$

$$\dot{m}_{\text{cond}} = 3\left(\frac{4\pi\left(1-\alpha_{\text{v}}\right)\eta_{\text{cd}}}{3\alpha_{\text{v}}}\right)^{1/3}\frac{\rho_{\ell}\rho_{\text{v}}\alpha_{\text{v}}\left(1-\alpha_{\text{v}}\right)}{\rho}\min\left(\left|\dot{R}_{\text{i}}\right|,\left|\overline{\dot{R}_{\text{t}}}\right|\right),$$

$$\text{where}\quad B = 4.193\times10^{9}\exp(-16.06\Delta T^{*}),\quad \eta_{\text{cd}} = 1.144\times10^{9}\exp(2.912\Delta T^{*}).$$

2.4 Accurate Capturing for Shock and Phase Interface

For stable and accurate shock capturing, a multi-dimensional limiting process (MLP) [35, 36] with RoeM_N or AUSMPW+_N convective flux [37] is used in this study. In terms of compatibility with the general form of EOS and numerical dissipation scaling for unsteady low-Mach number flows, the flux scheme [37] is an appropriate choice. Because bubble surface movement is predominant during bubble pulsation, the phase interface-sharpening technique LS-3MC [38] is employed to prevent excessive interface diffusion. The LS-3MC reconstructs the interface profile based on volume fraction gradients while preserving the total mass.

3 Computational Results

Extensive validations with field experimental references were performed to confirm that the proposed computational framework can capture the entire UNDEX process. Because there was no case where the entire process was measured in a single experiment, the validations are divided into two cases: Stage I, II (Shock wave and bulk cavitation) and Stage I, III (Shock wave and bubble pulsation). Table 2 contains a more detailed description of the validation cases. For all simulations, MLP-u2 limiter [36] with AUSMPW+_N flux scheme [37] is adopted for accurate and efficient shock capturing. The dual-time stepping method (BDF2) with block-LUSGS [39] is employed for the temporal discretization of the preconditioned system. The gravity source term is used for the buoyancy effect, and LS-3MC [38] using the Bézier curve reconstruction with $\epsilon = 0.45$ is applied to keep the phase interface sharp.

Table 2: Classification of validation problems.

	Classification	**Reference data**	**Flow physics**
Validation I	Numerical problem	Discontinuity location	Overall phenomena
Validation II	Field experiment	Pressure record	Shock wave (Stage I), Bulk cavitation (Stage II)
Validation III		Pressure record, Bubble radius record	Shock wave (Stage I), Bubble pulsation (Stage III)

3.1 Validation I: Theoretical Calculation

Before comparing with actual UNDEX experiments in earnest, the preliminary simulation is carried out on the two-dimensional small-scale problem [7]. This numerically configured test case represents the interaction scenario between the ocean surface and the underwater blast wave. The simulation is run on a 241 × 241 square grid system, with the initial condition provided from [7] as shown in Table 3.

Table 3: Initial condition of the validation case I.

Region	Pressure (Pa)	Density (kg/m^3)	Equation of State
Air	1.1×10^5	1.0	Ideal gas law
Water	Hydrostatic	997.0	Stiffened gas
Explosion bubble	9.12×10^8	1270.0	Ideal gas law

This problem is reduced to a two-phase situation because no phase change is taken into account, and the air property is used for the explosion bubble. As can be seen in Fig. 3, significant flow phenomena of UNDEX are well captured; primary shock wave, reflected expansion waves from the free surface, the rise of the free surface and expansion of the explosion bubble, etc. The time history of the flow discontinuity locations measured along the vertical center line is depicted in Fig. 4. The hollow and solid symbols represent the outcomes of theoretical calculation [7], and numerical simulation [40], respectively. The computation of this work shows good agreement with the prior simulation result, indicating that the developed computational framework can capture the overall UNDEX flow physics.

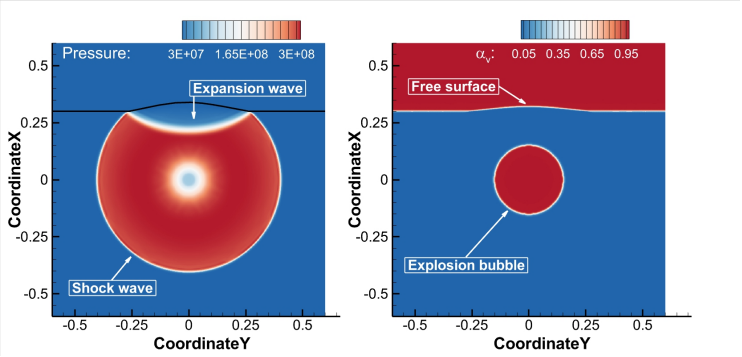

Figure 3: Pressure (right) and bubble volume fraction distributions at 15 ms.

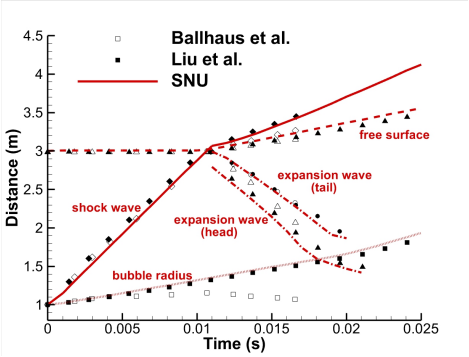

Figure 4: Comparison of flow discontinuity location

3.2 Validation II: Experiment with Bulk Cavitation

The experiment was designed to investigate the effect of underwater explosions on the survival of fish with swim bladders [9]. Among the many test runs in this field experiment, a specific case with the most significant amount of cavitation load reported is chosen as the reference for validation of Stages I and II (Shock wave and bulk cavitation, respectively). Table 4 contains a description of this experimental case.

Table 4: The description of Validation II.

Explosive material	Pentolite (50/50 TNT + PETN)
Charge weight	30.8 kg
Explosion depth	21.3 m
Sensor location	(Horizontal) 51.8 m from the detonation center (Vertical) 3.05 m beneath the free surface

3.2.1 Initial state for explosion gas bubble

The main driver of cavity generation is the primary shock wave. Thus, an accurate prediction of cavitation load begins with a correct estimation of the blast wave, emphasizing the importance of an appropriate initial condition setting. Because there is no specific scheme for directly establishing the initial bubble state, it must be discovered through trial and error to provide a realistic amount of shock load. The original sensor that recorded the shock wave intensity is located far away; therefore, the similitude relation [1, 41] is adopted for computational efficiency. The similitude relation is established by a number of UNDEX field experiments, which is a widely-used reference for the shock wave load. This equation provides the peak pressure value at a standoff distance D, when the charge weight of W is detonated:

$$p_{\max}(D) = 2.35 \times 10^4 \left(\frac{W^{1/3}}{D} \right)^{1.14} \text{ psi.} \tag{16}$$

The small-scale computational grid is generated with radial distributions and a domain boundary of 4 m. The measuring point of this study is set 1.5 m away from the detonation center since the similitude equation is valid from $D > 6R_{\text{initial}}$. To determine an appropriate grid resolution, four different levels of meshes are generated. Iteratively, the initial condition of the explosion bubble is determined, and the level 4 grid (Δs = 5 mm) demonstrated good agreement with the reference peak pressure as shown in Fig. 5; thus it is considered converged. These findings are utilized in the main simulation in Sect. 3.2.2.

3.2.2 Main simulation for Validation II

The computational mesh is generated with 7.1 million cells in total. The same level of grid resolution in Sect. 3.2.1 is retained in the region from the detonation center to the sensor location, and the grid cell size increases gradually to the far field. The domain size is expressed in the schematic diagram, Figure 6. In addition to the original sensor described in the report, supplementary sensors $S1$, $S2$, and $S3$ are virtually assigned. Initial flow conditions and equations of state for the corresponding region are summarized in Table 5.

Table 5: Initial condition of the Validation II.

Region	Pressure (Pa)	Temperature (K)	Density (kg/m^3)	Equation of State
Air	101325.0	300.0	1.0	Ideal gas law
Water (liquid)	Hydrostatic	300.0	997.0	IAPWS97 (liquid)
Water (vapor)	-	-	-	IAPWS97 (vapor)
Explosion bubble	3.394×10^9	1880.0	1180.34	JWL

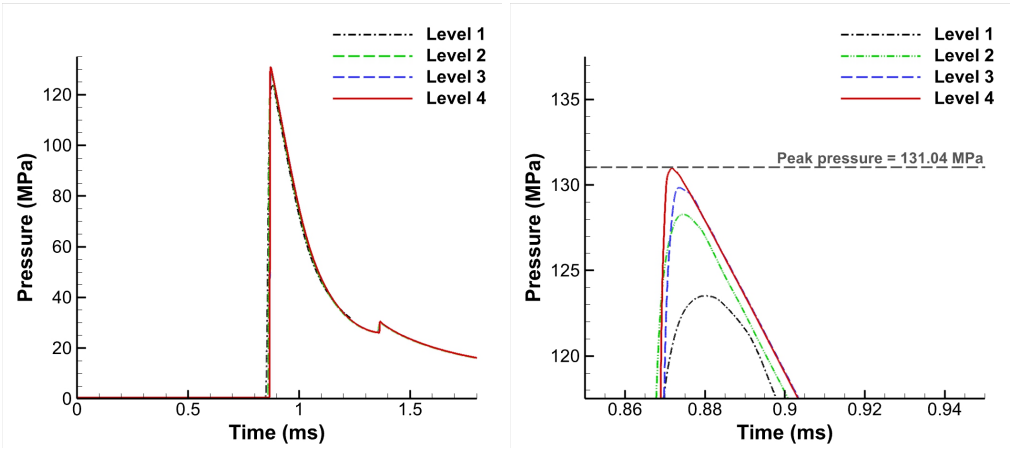

Figure 5: Pressure history by different grid levels (standoff distance 1.5 m).

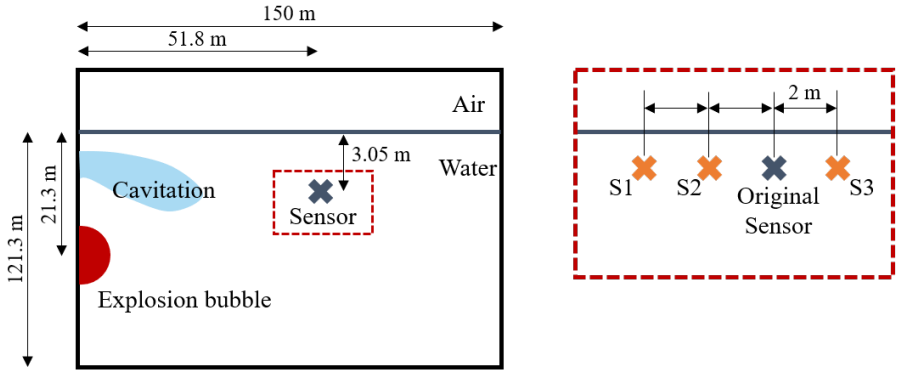

Figure 6: Schematic diagram of Validation II.

The initial bubble radius, $R_0 = 0.184$m, is then obtained from the mass conservation of explosive charge and spherical form assumption of explosion gas bubble. For the thermodynamic cavitation process, the physics-based cavitation model [34] is used in this work. The physical time step 1.0×10^{-7}s is adopted for the simulation.

Figure 7 shows the pressure distribution of the flow field, with the gray-colored area indicating the cavity region, where the local pressure is less than the saturation pressure. The major flow phenomena of UNDEX are well captured as expected. As the blast wave reaches the free surface, expansion waves reflect into the water and a weak shock wave is transmitted into the air medium (Figs. 7(a) and (b)). The vapor cavity forms in the low-pressure region (Figs. 7(b)-(e)), and then collapses (Fig. 7(f)), triggering the bulk cavitation loading or the secondary shock waves (Fig. 7(g) and (h)). Multiple weak pressure waves near the free surface are induced by consecutive local cavity collapses.

Figure 8 depicts the pressure-time history measured at the sensors. The simulation result at the original sensor location is represented by the solid green line. The primary shock loading is nearly identical to the experimental data, indicating that the initial condition found in Sect. 3.2.1 is satisfactory. The arrival of the secondary loading is comparable, but the duration and peak value differs from the reference. The red solid, orange, and blue dashed lines are the pressure history measured at the supplementary sensor locations $S1$ to $S3$, respectively. Each of the sensors is located at just 2 to 4 m away from the original sensor as in Fig. 6. The duration and the peak value of the bulk cavitation loading of these points are highly disparate, but sensor 1 gives remarkably better predictions compared to the original sensor location. This unsteadiness comes from the interaction of shock waves generated by instantaneous cavity collapse at multiple locations.

According to the field experiment report, the measuring point is located beneath the buoy and is connected by a steel wire over 100 m. This experimental setup introduces a certain level of uncertainties about the precise sensor location. Furthermore, the local flow field is unsteady enough to show a significant disparity in results only a few meters away from the original sensor position. Given the possibility that the measuring point can be easily moved by the current and the local flow phenomena is highly unsteady, the computational framework has been thoroughly validated using the field experimental data.

3.2.3 Effect of thermodynamic cavitation process

Additional simulation with the pressure-cut model is performed to investigate the efficacy of the thermodynamic cavitation process in predicting the bulk cavitation load (Eq. 14). Figure 9 shows the pressure distribution of pressure-cut simulation alongside the thermodynamic cavitation process result. A gray-colored area indicates the cavity region, where local pressure is less than the saturation value.

The computed pressure distributions are significantly different. In terms of the intensity and time incidence of cavity collapse, the result with a pressure-cut model gives a mild and early breakdown of the cavity region (Figs. 9(a)-(d)), whereas the thermodynamic cavitation process shows much delayed and drastic collapse which is closer to the experimental data (Figs. 9(a′)-(d′)). Furthermore, the vapor cavity breaks down near the centerline with the pressure-cut model, whereas the cavitation region by the thermodynamic cavitation model collapses about 35 m horizontally away from the centerline. The difference is easily discernible

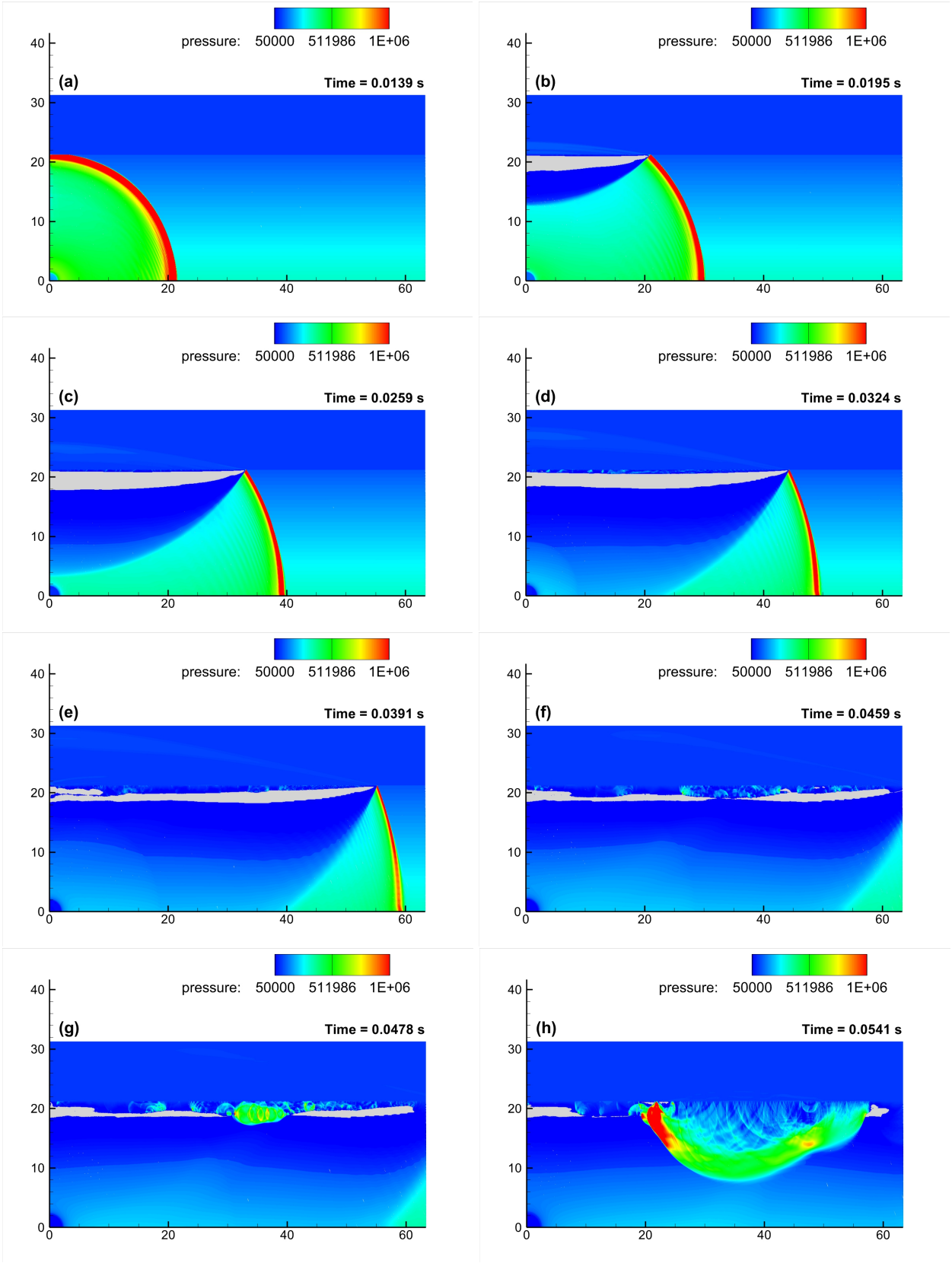

Figure 7: Pressure field of the main simulation for Validation II.

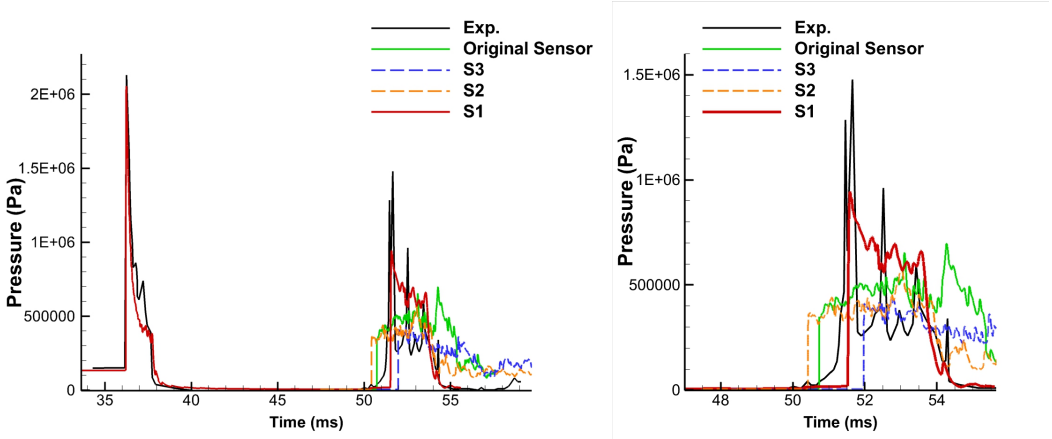

Figure 8: Pressure history measured at the sensors.

from the pressure history measured at the sensor, as shown in Fig. 10.

The pressure-cut model and the thermodynamic cavitation model produced the green and red solid lines, respectively. The red line represents the result obtained at a distance of 4 m from the original sensor position ($S1$ in Fig. 8). According to the pressure-cut model, the bulk cavitation loading arrives at 43.53 ms with an intensity of more or less hydrostatic pressure, which is premature as well as weak strength in comparison to the experimental data. This discrepancy stems from the way the cavitation process is described. At the moment of cavity collapse, an instantaneous mass transfer from the vapor to liquid releases energy (Fig. 11), thereby, much stronger pressure waves are induced. It is thus confirmed that the thermodynamic cavitation process gives a better prediction of the bulk cavitation loading in terms of arrival time, duration, and intensity. Table 6 summarizes the accurate figures for both simulations.

Table 6: Summary of computation results in Validation II (relative error in parenthesis).

	Pressure-cut model	**Thermodynamic cavitation process**
Shock loading	2.05 MPa (3.31%)	2.05 MPa (3.31%)
Bulk cavitation loading	102.6 kPa (93.1%)	944.1 kPa (36.1%)
Moment of cavitation load	43.53 ms (15.4%)	51.54 ms (0.56%)

3.3 Validation III: Experiment for Bubble Pulsation

The experiment was carried out to record the changes in the explosion bubble size with various charge weight and depth conditions [8]. In this study, the validation of the computational framework for UNDEX Stage I and III (shock wave and bubble pulsation, correspondingly) is conducted. Additional simulation for the half-depth condition is performed to compare the buoyancy effect on the bubble dynamics. A description of this experimental case is in Table 7.

A study of the initial bubble condition and grid convergence were also carried out but were omitted for brevity. The computational grid is generated by the same topology described in Sect. 3.2.1, with a domain

Table 7: The description of validation III.

Explosive material	TNT
Charge weight	0.227 kg
Explosion depth	182.88 m / 91.44 m
Sensor location	0.69 m (identical depth with explosive)

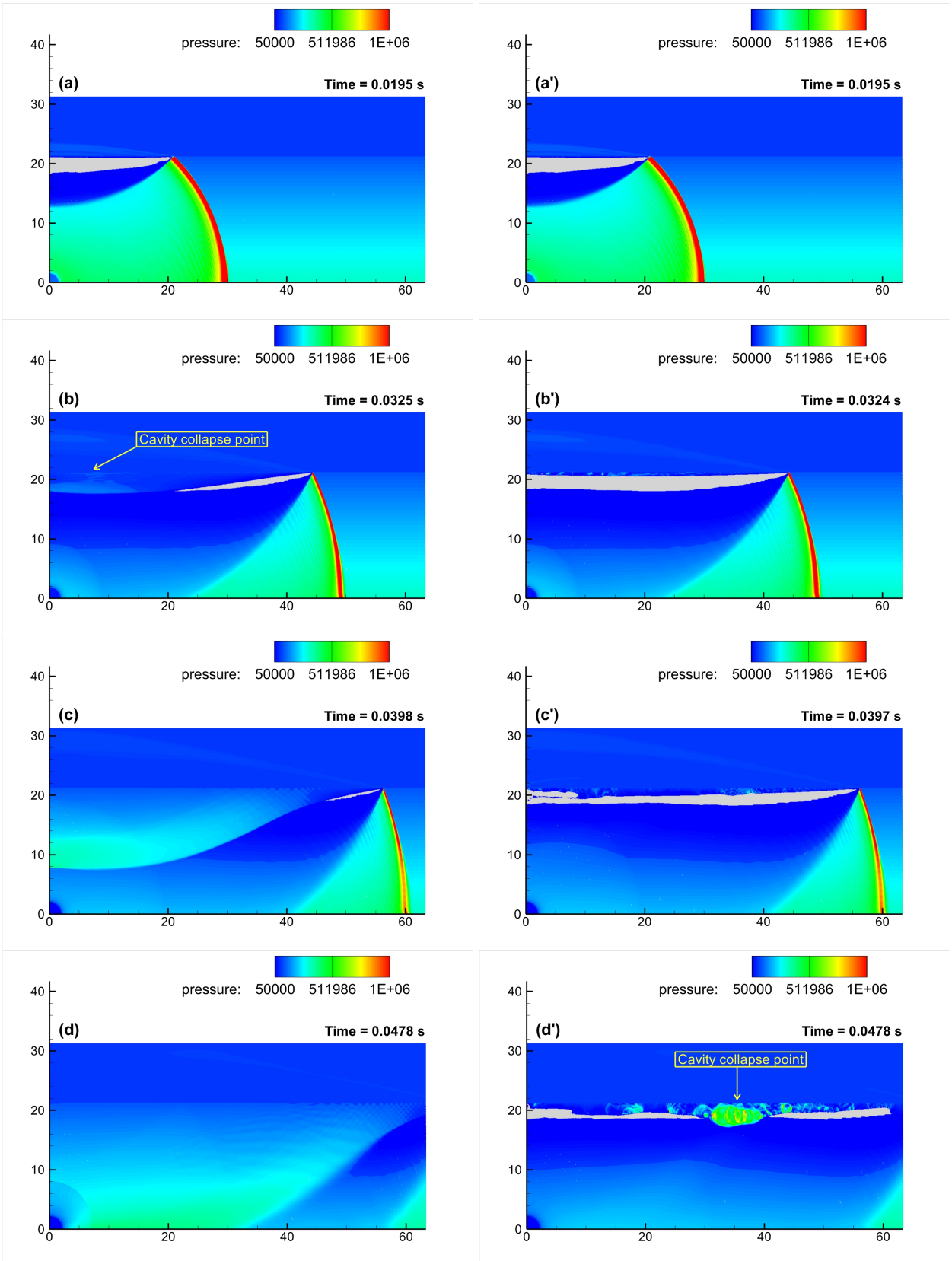

Figure 9: Comparison of pressure-cut model (left column) and thermodynamic cavitation process results (right column).

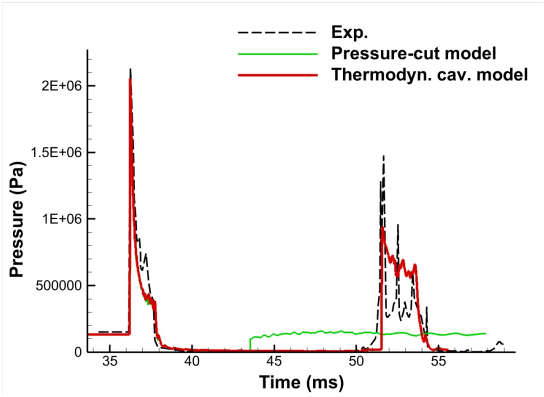

Figure 10: Comparison of cavitation models in Validation II.

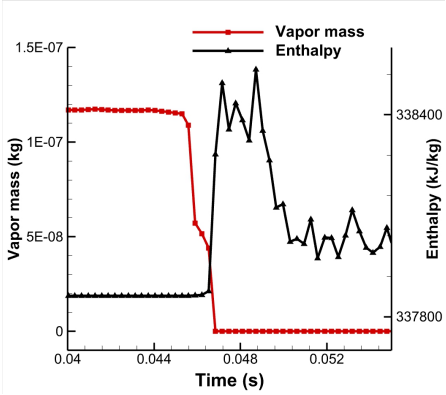

Figure 11: Vapor mass fraction and specific enthalpy distribution at the cavity collapse point.

size is 50 m radial and a total of 1.5 million cells. The mesh is clustered at the bubble dynamics region with $\Delta s = 0.002$ m and the grid cell size increases gradually to the far field. The initial state of the bubble is discovered to provide a realistic amount of shock load and bubble dynamic behavior. Table 8 is the configured initial condition and equations of state to the corresponding region.

Table 8: Initial condition of the validation III.

Region	Pressure (Pa)	Temperature (K)	Density (kg/m^3)	Equation of State
Water	Hydrostatic	300.0	997.0	IAPWS97
Explosion bubble	1.8×10^9	2000.0	982.35	JWL
Explosion bubble (half-depth)	2.5×10^9	2200.0	1098.37	JWL

The initial bubble radius is calculated to be $R_0 = 0.0381$ m. For half-depth condition, the initial radius is $R_0 = 0.0367$ m. Because the explosion occurred in deep water, the simulation is based on a two-phase scenario (liquid water and non-condensable gas phases). The phase change usually occurs at the liquid adjacent to the high-temperature bubble surface. In contrast to the spark-generated UNDEX situation, the detonation-generated bubble is formed with non-condensable explosion gas, and the phase change effect is marginal to the bubble dynamic behavior. As a result, no phase change process is adopted in this validation. The physical time step used is identical to Sect. 3.2.2.

The bubble pulsation in the UNDEX scenario proceeds with the following mechanism. A high internal pressure drives the surrounding fluid outward, and the bubble begins to expand. The bubble over-expands as it grows due to inertia, and the internal pressure becomes lower than the periphery. Relatively higher hydrostatic pressure accelerates the bubble to collapse until the compressibility of the gas bubble can withstand it and then rebounds. The sequence of events is continuously repeated until the bubble's energy is depleted. Figure 12 shows the time distribution of the pressure field and bubble volume fraction at a depth of 182.88 m. As can be seen, the initial shock wave (Stage I) propagates in a very short time scale while the bubble slowly expands (Fig. 12(b)). The internal pressure of the bubble is lower than the surrounding water at the moment of maximum expansion, and begins to contract (Figs. 12(c) and (d)). Two particular physical phenomena are captured at the rebound moment; the pressure wave that leads to the bubble pulsation load and Rayleigh-Taylor interfacial instability (Figs. 12(e) and (f)). Rayleigh-Taylor instability is a physical phenomenon at the interface between two fluids of different densities, which occurs when the lighter fluid pushes the heavier fluid. Due to the phase interface maintaining the sharp representation, even very localized flow physics is captured.

Figure 13 indicates the history of bubble radius and shock waves measured at the sensor, where the solid red and dashed blue lines are the results of 182.88 m and 91.44 m depths, respectively. The experimental data for the shock wave history is available only for the former condition, and the bubble radius is provided

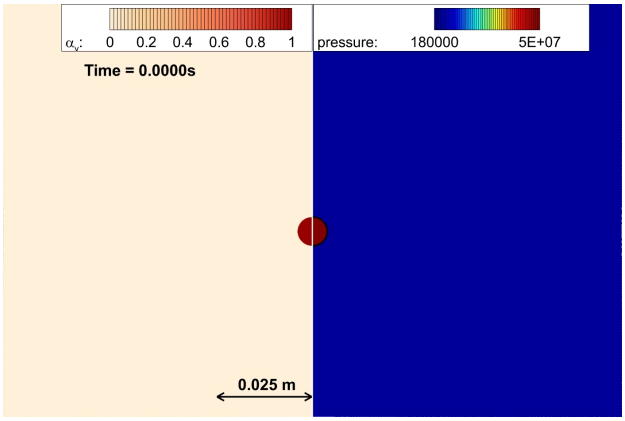

(a) Initial state.

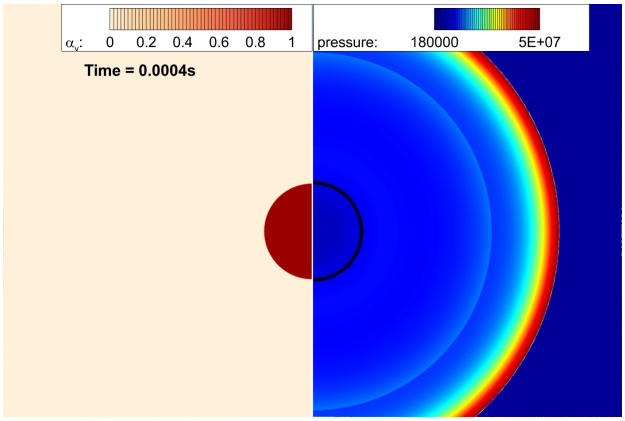

(b) Bubble expansion moment.

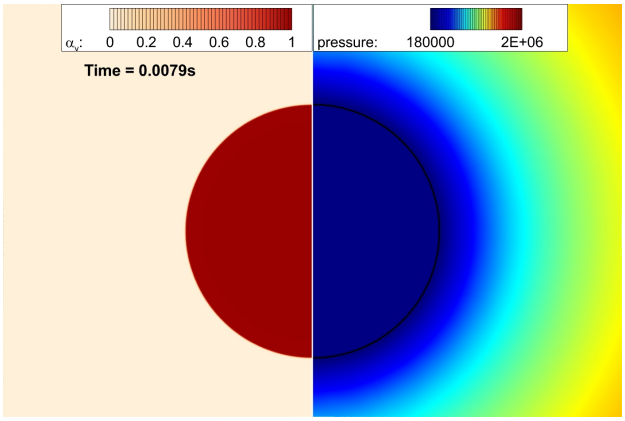

(c) Maximum bubble moment.

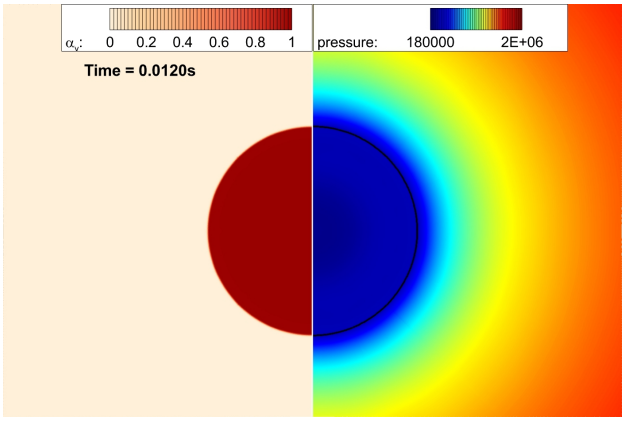

(d) Bubble contraction moment.

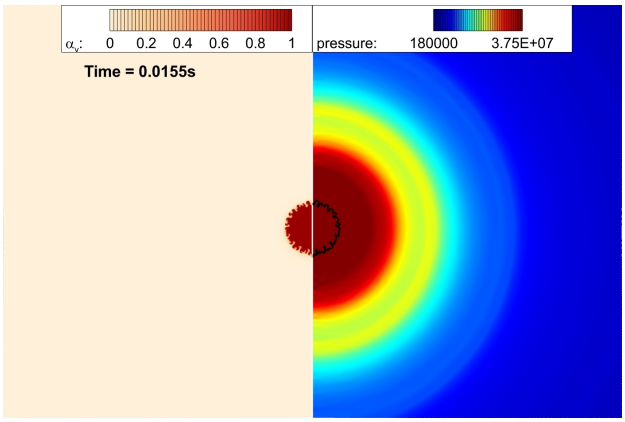

(e) Bubble collapse moment.

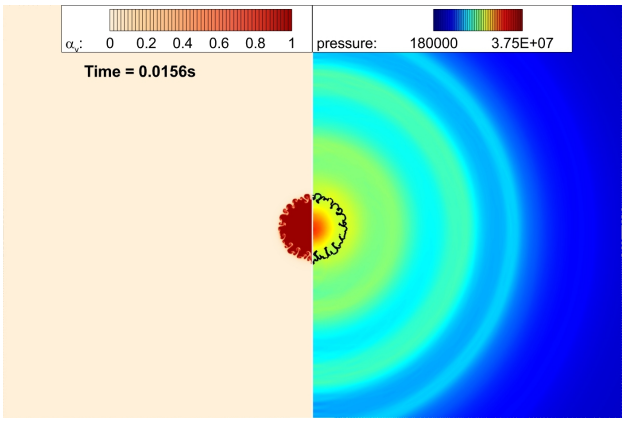

(f) Bubble rebound moment.

Figure 12: Pressure and bubble volume fraction distribution of Validation III.

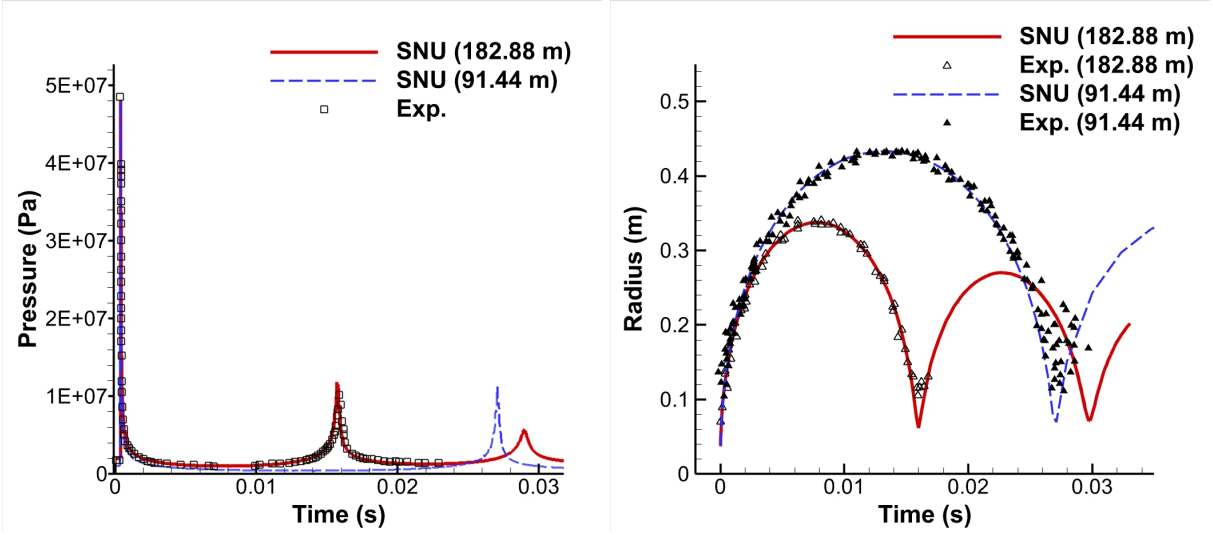

(a) Pressure history (standoff distance 0.69 m).

(b) Bubble radius history.

Figure 13: Pressure and bubble radius history of Validation III.

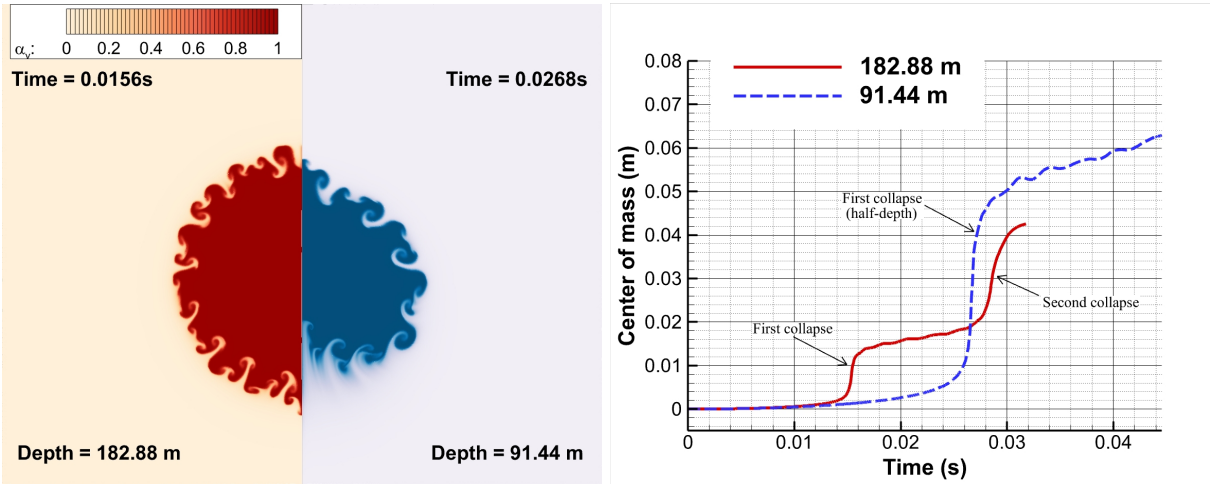

(a) Volume fractions at the bubble collapse moment.

(b) Time history of the bubble's center of mass.

Figure 14: Comparison of the bubble dynamics by depth.

for the first period. The computation yields good agreements for the primary shock wave (Stage I), bubble pulsation (Stage III), and subsequent bubble pulse load. In particular, the bubble pulse intensity is often under-predicted when the ideal gas EOS is employed for the explosion bubble, although the bubble radius history is well captured. The bubble pulse load result implies that the present computation appropriately reflects the energy transmission at the bubble rebound moment. At the half-depth condition, the bubble expands to a greater extent since the ambient pressure is relatively lower than the deep water. The detonation depth affects other aspects of bubble behavior. Figure 14 shows the comparison of the bubble dynamics by depth conditions. The rebound bubble has a nearly symmetrical shape at 182.88 m, while an asymmetrical topology is observed at the half-depth, as shown in Fig. 14(a). The asymmetric bubble shape comes from a greater expansion which induces a larger difference in hydrostatic pressure between the top and bottom of the bubble, thereby pushing upward with more considerable fluid force. The center of the bubble mass by time is depicted in Fig. 14(b). Though the bubble becomes buoyant as it expands, the fluid drag force resists the upward migration. At the moment of collapse, however, an inward fluid flow and buoyancy become larger

than the drag, and the bubble rapidly moves vertically. The migrated distance during the first and second collapses at 182.88 m depth are 0.015 m and 0.024 m, respectively. In the half-depth condition, the bubble migrated 0.05 m which exceeds the total distance traveled by the former case during the two rebounds.

Since the sharp representation of the phase interface is maintained and the computation appropriately reflects the bubble energy transmission, macroscopic as well as microscopic bubble behavior is well predicted: overall bubble dynamics and interfacial instability. Compared to actual experiment records, the proposed computational framework demonstrates the capability to capture the critical physics of the entire UNDEX process.

4 Conclusion and Future Work

A high-fidelity computational framework is developed to simulate the entire process of underwater explosion: initial shock wave (Stage I), bulk cavitation (Stage II), and pulsation of explosion bubble (Stage III). The proposed requirements for the framework are as follows:

- A multi-phase flow model capable of handling at least four phases/species: liquid water, water vapor, explosion gas, and air above the free surface.
- A general form of equation of state that provides accurate thermodynamic properties across a wide range of flow conditions
- A thermodynamic cavitation process that can model the actual generation of vapor phase with latent heat exchange.
- Accurate and efficient numerical methods for capturing multi-phase shock waves and sharpening of phase interfaces.

In this work, the in-house program ACTFlow_MP is developed in accordance with the proposed requirements.

A theoretical UNDEX calculation and two actual field test records are used to validate the proposed numerical framework. As a preliminary, the program shows good agreement for capturing the overall UNDEX phenomena compared to theoretical calculation: shock wave propagation into the water and air, bubble expansion, etc. Because no single experimental case involves all three stages of UNDEX, the validation is done separately. The second validation result shows that the computational framework predicts the shock wave and bulk cavitation (Stage I and II, correspondingly). It is also shown that the thermodynamic cavitation process is essential in capturing the bulk cavitation loading compared to the simple pressure-cut model. The numerical results from the third validation case give good agreement in predicting the shock wave and bubble pulsations (Stage I and III, respectively). Rayleigh-Taylor instability and bubble pulse load emission are clearly visible at the time of bubble collapse.

By adopting the developed computational framework, a couple of future works will be carried out: initial state modeling for the explosion bubble and the nonlinear flow physics investigation in multiple explosions. The underwater explosion is basically an initial value problem; therefore, establishing the initial bubble condition that provides physical flow phenomena is critical. Multiple underwater explosions are a specific problem in which all of the physical phenomena mentioned above interact significantly (Stage I-III). As a next step, nonlinear interactions between multiple explosion bubbles will be investigated.

Acknowledgments

This research is supported by Korea Institute of Science and Technology and Information (KSC-2020-CRE-0220), by Institute of Advanced Aerospace Technology, and by the United States Office of Naval Research (ONR) and ONR Global (N62909-20-1-2085), and monitored by Dr. Daniel Tam and Dr. Sung-Eun Kim.

References

[1] R. H. Cole and R. Weller. Underwater explosions. *Physics Today*, 1(6):35, 1948.

[2] Lord Rayleigh. Viii. on the pressure developed in a liquid during the collapse of a spherical cavity. *The London, Edinburgh, and Dublin Philosophical Magazine and Journal of Science*, 34(200):94–98, 1917.

[3] M. S. Plesset. The dynamics of cavitation bubbles. *Journal of Applied Mechanics*, 1949.

[4] F. R. Gilmore. The growth or collapse of a spherical bubble in a viscous compressible liquid. 1952.

[5] A. Lezzi and A. Prosperetti. Bubble dynamics in a compressible liquid. part 2. second-order theory. *Journal of Fluid Mechanics*, 185:289–321, 1987.

[6] F. Hegedűs, C. Hős, and L. Kullmann. Influence of heat transfer on the dynamic response of a spherical gas/vapour bubble. *International journal of heat and fluid flow*, 31(6):1040–1049, 2010.

[7] W. F. Ballhaus Jr. and M. Holt. Interaction between the ocean surface and underwater spherical blast waves. *The Physics of Fluids*, 17(6):1068–1079, 1974.

[8] E. Swift Jr. and J. C. Decius. Measurement of bubble pulse phenomena, iii. radius and period studies. Technical report, Office of Naval Research (ONR), 1950.

[9] J. B. Gaspin. Experimental investigations of the effects of underwater explosions on swimbladder fish. i. 1973 chesapeake bay tests. Technical report, Naval Surface Weapons Center White Oak Lab Silver Spring MD, 1975.

[10] P. Cui, A. M. Zhang, and S. P. Wang. Small-charge underwater explosion bubble experiments under various boundary conditions. *Physics of Fluids*, 28(11):117103, 2016.

[11] E. Klaseboer, K. C. Hung, C. Wang, C. W. Wang, B. C. Khoo, P. Boyce, S. Debono, and H. Charlier. Experimental and numerical investigation of the dynamics of an underwater explosion bubble near a resilient/rigid structure. *Journal of Fluid Mechanics*, 537:387–413, 2005.

[12] L. Gannon. Submerged aluminum cylinder response to close-proximity underwater explosions–a comparison of experiment and simulation. *International Journal of Impact Engineering*, 133:103339, 2019.

[13] S. A. Wilkerson. Boundary integral technique for explosion bubble collapse analysis. Technical report, Army Research Lab Aberdeen Proving Ground MD, 1993.

[14] C. Wang, B. C. Khoo, and K. S. Yeo. Elastic mesh technique for 3d bim simulation with an application to underwater explosion bubble dynamics. *Computers and Fluids*, 32(9):1195–1212, 2003.

[15] Z. Jin, C. Yin, Y. Chen, and H. Hua. Numerical study on the interaction between underwater explosion bubble and a moveable plate with basic characteristics of a sandwich structure. *Ocean Engineering*, 164:508–520, 2018.

[16] S. Li, A.-M. Zhang, R. Han, and P. Cui. Experimental and numerical study of two underwater explosion bubbles: Coalescence, fragmentation and shock wave emission. *Ocean Engineering*, 190:106414, 2019.

[17] G. Wang, S. Zhang, M. Yu, H. Li, and Y. Kong. Investigation of the shock wave propagation characteristics and cavitation effects of underwater explosion near boundaries. *Applied Ocean Research*, 46:40–53, 2014.

[18] A. Daramizadeh and M. R. Ansari. Numerical simulation of underwater explosion near air–water free surface using a five-equation reduced model. *Ocean Engineering*, 110:25–35, 2015.

[19] O. Haimovich and S. H. Frankel. Numerical simulations of compressible multicomponent and multiphase flow using a high-order targeted eno (teno) finite-volume method. *Computers and Fluids*, 146:105–116, 2017.

[20] M. Pelanti and K.-M. Shyue. A numerical model for multiphase liquid–vapor–gas flows with interfaces and cavitation. *International journal of multiphase flow*, 113:208–230, 2019.

[21] J. Yu, J. Liu, H. Wang, J. Wang, L. Zhang, and G. Liu. Numerical simulation of underwater explosion cavitation characteristics based on phase transition model in compressible multicomponent fluids. *Ocean Engineering*, 240:109934, 2021.

[22] A. B. Wardlaw Jr and H. U. Mair. Spherical solutions of an underwater explosion bubble. *Shock and Vibration*, 5(2):89–102, 1998.

[23] L. Hai and X. Ren. Computational investigation on damage of reinforced concrete slab subjected to underwater explosion. *Ocean Engineering*, 195:106671, 2020.

[24] H. Kim, Y. Choe, D. Min, and C. Kim. Methods for compressible multiphase flows and their applications. *Shock Waves*, 29(1):235–261, 2019.

[25] C. Lee, E. Kim, K. Yune, and C. Kim. Actflow: A target-oriented finite volume solver for all-speed

compressible turbulent flow simulations. In *AIAA Scitech 2021 Forum*, page 1533, 2021.

[26] E.A. Brujan, T. Ikeda, K. Yoshinaka, and Y. Matsumoto. The final stage of the collapse of a cloud of bubbles close to a rigid boundary. *Ultrasonics Sonochemistry*, 18(1):59–64, 2011.

[27] M. Tinguely. The effect of pressure gradient on the collapse of cavitation bubbles in normal and reduced gravity. Technical report, EPFL, 2013.

[28] J. M. Weiss and W. A. Smith. Preconditioning applied to variable and constant density flows. *AIAA Journal*, 33(11):2050–2057, 1995.

[29] W. Wagner and H.-J. Kretzschmar. Iapws industrial formulation 1997 for the thermodynamic properties of water and steam. *International steam tables: properties of water and steam based on the industrial formulation IAPWS-IF97*, pages 7–150, 2008.

[30] E. L. Lee, H. C. Hornig, and J. W. Kury. Adiabatic expansion of high explosive detonation products. Technical report, Univ. of California Radiation Lab. at Livermore, Livermore, CA (United States), 1968.

[31] L. Donahue, F. Zhang, and R. C. Ripley. Numerical models for afterburning of tnt detonation products in air. *Shock Waves*, 23(6):559–573, 2013.

[32] R. E. Shear. Detonation properties of pentolite. Technical report, Army Ballistic Research Lab Aberdeen Proving Ground MD, 1961.

[33] D. L. Miller, J. C. Schoof, and M. L. Hobbs. Thermochemical plots using jczs2i piece-wise curve fits. Technical report, Sandia National Lab.(SNL-NM), Albuquerque, NM (United States), 2013.

[34] H. Kim and C. Kim. A physics-based cavitation model ranging from inertial to thermal regimes. *International Journal of Heat and Mass Transfer*, 181:121991, 2021.

[35] J. S. Park, S.-H. Yoon, and C. Kim. Multi-dimensional limiting process for hyperbolic conservation laws on unstructured grids. *Journal of Computational Physics*, 229(3):788–812, 2010.

[36] J. S. Park and C. Kim. Multi-dimensional limiting process for finite volume methods on unstructured grids. *Computers and Fluids*, 65:8–24, 2012.

[37] H. Kim, H. Kim, and C. Kim. Computations of homogeneous multiphase real fluid flows at all speeds. *AIAA journal*, 56(7):2623–2634, 2018.

[38] H. Kim and C. Kim. Extension of ausm-type fluxes: from single-phase gas dynamics to multi-phase cryogenic flows at all speeds. *Shock Waves*, 29(5):735–753, 2019.

[39] R. F. Chen and Z. J. Wang. Fast, block lower-upper symmetric gauss-seidel scheme for arbitrary grids. *AIAA journal*, 38(12):2238–2245, 2000.

[40] T. G. Liu, B. C. Khoo, and K. S. Yeo. The simulation of compressible multi-medium flow: Ii. applications to 2d underwater shock refraction. *Computers and Fluids*, 30(3):315–337, 2001.

[41] C. R. Niffenegger. Revised similitude equations for the underwater shock-wave performance of pentolite and hbx-1. Technical report, Naval Ordnance Lab White Oak MD, 1961.